

ORIGINAL RESEARCH ARTICLE

Multi-objective optimization of intense pulsed light sintering process for aerosol jet printed thin film

Guo Liang Goh^{1†}, Haining Zhang^{2†}, Guo Dong Goh¹, Wai Yee Yeong^{1*}, Tzyy Haur Chong^{3,4}

¹Singapore Centre for 3D Printing, School of Mechanical and Aerospace Engineering, Nanyang Technological University, Singapore

²Department of Intelligent Manufacturing, School of Information Engineering, Suzhou University, Suzhou, China

³Singapore Membrane Technology Centre, Nanyang Environment & Water Research Institute, Nanyang Technological University, Singapore

⁴School of Civil and Environmental Engineering, Nanyang Technological University, Singapore

Abstract

The sintering of printed nanoparticle films is a necessary processing step for most nanoparticle inks to make the printed film functional. The sintering of nanoparticle is usually performed through thermal sintering, photonic sintering, induction sintering, etc. Intense pulsed light (IPL) sintering method is one of the most popular sintering methods for nanoparticle inks due to the fast and effective process, but it may yield mediocre performance if improper sintering parameters are used. In this work, we investigate the correlation between the two factors which are the print passes of aerosol jet printing and the sintering distance of the samples on the effect of the surface morphology and sheet resistance. A contradictory correlation between the two factors was observed and a multi-objective optimization was carried out using machine learning method to identify the most optimum conditions for both factors. We found that multi-objective optimization approach is effective in reducing the conflicting responses, thus the sintered thin film can have low sheet resistance and low surface roughness. This work provides an essential guide for achieving conductive films with electrical conductivity and low surface roughness using IPL sintering process for fast fabrication of multi-layered electronics such as electrochemical electrodes.

Keywords: Additive manufacturing; 3D printing; Printed electronics; Multi-objective optimization; Photonic sintering; Process optimization

†These authors contributed equally to this work

***Corresponding author:**

Wai Yee Yeong
(wyyeong@ntu.edu.sg)

Citation: Goh GL, Zhang H, Goh GD, *et al.*, 2022, Multi-objective optimization of intense pulsed light sintering process for aerosol jet printed thin film. *Mater Sci Add Manuf.* 1(2): 10.

<http://doi.org/10.18063/msam.v1i2.10>

Received: March 31, 2022

Accepted: May 10, 2022

Published Online: June 22, 2022

Copyright: © 2022 Author(s). This is an Open Access article distributed under the terms of the Creative Commons Attribution License, permitting distribution, and reproduction in any medium, provided the original work is properly cited.

Publisher's Note: Whioce Publishing remains neutral with regard to jurisdictional claims in published maps and institutional affiliations.

1. Introduction

In the past decade, printed electronics technology has received great attention because of the increasing needs for alternative electronics fabrication technology to produce unconventional electronics, especially in the field of flexible and stretchable electronics^[1,2]. Conventionally, electronics are manufactured using silicon wafer

technology that requires high processing temperature which poses restrictions on the material options^[3]. In contrast, printed electronics technology uses functional inks to create circuits and electronic components, thereby lowering the process temperature and creating more opportunities for new electronic architectures with various substrates, particularly for low thermal stability substrates^[4-7]. It has allowed for new opportunities for the creation of flexible electronic components that can be used in applications such as water technology for system health monitoring purpose^[8].

In the early years, printed electronics is normally done using traditional additive-based printing techniques that require tool, mask, or stencil for the patterning of inks^[9]. These traditional printing techniques include screen printing, gravure printing, flexographic printing, and offset printing. These techniques are compatible with the roll-to-roll manufacturing process and allow the use of flexible substrates, which makes them highly suitable for mass production of flexible electronics. However, the recent shift in the industry's needs for custom-made electronics has spurred the search for cheaper alternatives for electronic fabrication because of the high initial cost for the tools and stencils renders the traditional printing techniques uneconomic for such purpose. In contrast, three-dimensional (3D) printing, also known as additive manufacturing, is found to be a better option for the fabrication of highly customizable advanced electronics^[10]. At present, 3D printing techniques such as inkjet printing^[11], aerosol jet printing^[12-15], and direct ink writing^[16] have been increasingly used by the industry to manufacture advanced electronics that require fine resolution and sophisticated geometry. Among which, aerosol jet printing technique has gained much attraction over the years due to its capability to process a wide range of materials and the high printing resolution^[17]. Besides, it can also be used to integrate electronics on 3D structures, making it suitable for realizing novel electronic designs^[18].

Regardless of the printing techniques, the functional inks remain the key ingredient to achieving the low processing temperature for printed electronics^[19,20]. To date, various types of functional inks such as silver nanoparticle inks, gold nanoparticles inks, and silver nanowire inks have been developed to cater for different applications^[4,21,22]. Functional inks generally contain several components, namely, the active material, the solvent, the binder, the surfactant, and other additives^[20]. The active materials and binder made up the main materials of the printed layers that determine the type and property of the layers, whereas the other materials such as the solvent, surfactant, and other additives will be removed in the sintering process.

In general, a sintering treatment is required to process the printed ink layers in order to make the active materials functional^[23]. This is because the active materials are normally covered with a layer of organic stabilizer, which impedes their functionality. Sintering treatment removes the organic stabilizer layer and binds the active materials together. For the case of metal nanoparticle, the nanoparticles receive energy during the sintering process and fuse together and grow larger to form a conductive network of nanoparticles. Besides, sintering treatment also enhances the adhesion of the printed materials to the substrates. Till now, there are many different sintering techniques that have been developed such as thermal sintering^[24], electrical sintering^[25], induction sintering^[26], and photonic sintering^[27]. Each sintering technique offers its unique advantages and possesses certain limitations. For examples, thermal sintering treatment can achieve homogeneous sintering but may not be suitable for all substrates as the substrate will be exposed to the same sintering condition. In contrast, induction sintering and electrical sintering offer selective sintering of nanoparticle layers, but only work with metallic inks and require pre-thermal treatment to make them conductive.

Intense pulsed light (IPL) sintering is a type of photonic sintering method that uses pulses of high intensity light to sinter the nanoparticle inks^[28]. The process uses a xenon lamp that emits a broad spectrum of light with wavelength ranges from visible light to UV light as the energy source^[29-31]. Unlike other sintering techniques, IPL sintering can be done in a very short time and does not induce significant damage to the substrates. The performance of the IPL sintering technique depends on various factors such as the light intensity, the type of substrates, the ink composition, the light absorption of the nanoparticle, and the thickness of the printed film. Despite the advantages of IPL technique, it is widely known that the process can cause defects such as cracks and delamination of the printed film due to the rapid vaporization of the gases originating from the organic compounds^[32]. These defects can cause undesirable and inconsistent performance of the electrical circuit or electronics components. Severe delamination can also restrict the use of the IPL-sintered conductive film for multilayer electronic designs which requires additional insulating or functional layers atop of the printed conductive film such as the case of electrochemical sensing electrodes. Although this issue can be solved by using back irradiation rather than top irradiation, it is only limited to transparent substrate^[31] and does not address the issue for some samples that requires top irradiation. Although preheating the samples is found to be helpful in reducing delamination in certain cases, it may not solve the issue entirely for thicker samples^[33].

In this work, we explore the use of IPL sintering technique for sintering aerosol jet printed silver nanoparticle film for printed electronics applications. Although there have been many works that investigate the effect of various process parameters on the performance silver nanoparticle film^[34-39], no study has investigated the interplay between the sintering parameters and film thickness on the quality and the performance of the sintered film. The objective of this work is to find out the process window of the IPL sintering process to achieve crack-free films with low sheet resistance for aerosol jet printed film with different thicknesses. To better analyze the correlation between different factors such as sintering distance and print passes on the surface morphology and electrical property of the printed film, a multi-objective optimization method was adopted. Here, a modified central composite design (CCD) was used to study the relationships between the quality of the sintered films and the main printing and sintering parameters. Analysis of variance (ANOVA) was conducted to examine individual effects and the interactions of the main variables on the sheet resistance and surface roughness of the sintered thin films. The results of analysis suggest that the CCD-derived models are statistically meaningful. The modified CCD-derived models were then optimized by a desirability function method, and a 2-dimensional (2D) optimal printing and sintering window were determined to yield thin film with low sheet resistance and low surface roughness. Following that, the derived statistical models were jointly driven with a non-dominated sorting genetic algorithm (GA) to systematically optimize the conflicting responses in a more robust manner. The findings demonstrate the effectiveness of the suggested multi-objective optimization approach in reducing the conflicting responses. This work presents useful guide for future attempts to optimize the IPL sintering parameters for various nanoparticle-based film such as gold for good electrical conductivity and low surface roughness for fast fabrication of multi-layered electronics such as electrochemical electrodes.

2. Materials and methods

2.1. Materials

The silver nanoparticle ink that was used in this work is UT Dots Ag40TE purchased from UT Dots[®]. The silver nanoparticle is reported to have an average particle diameter of 10 nm and it is dispersed in proprietary solvents. The optimum sintering temperature of the ink using conventional thermal sintering method is claimed to range from 150°C to 200°C for at least 30 min. For the substrate, Kapton[®] polyimide films with a thickness of 75 µm were used for the fabrication of test coupons.

Polyimide substrate was used in this work because it is widely used in the field of printed electronics for the fabrication of flexible electronics and wearables due to the good material property and thermal compatibility. The polyimide substrate was first cleaned with soap water and ethanol to remove the inorganic and organic contaminants on its surface. This was done to ensure that the surface wettability of the surface was uniform to ensure consistent print quality and film adhesion. No surface modification was done on the polyimide substrate.

2.2. Fabrication of test coupons

Each test coupon is made up of four conductive thin film printed on polyimide films which can ensure at least a sample size of $n = 3$ for each test condition for statistically meaningful analysis. The diameter of the coupon is 1 cm. The tool path for the print head is designed to have a line pitch of 120 µm to ensure sufficient overlapping between the adjacent lines for formation of homogeneous film. A spiral tool path design was used for the 1 cm diameter circles. The printing of ink was done using an Optomec[™] Aerosol jet[®] 5X system (Figure 1A). Ultrasonic atomizer was used for the printing of silver ink. For good printability, the process parameters for printing the silver ink onto the polyimide film were optimized to be as follows: sheath flow = 20 standard cubic centimeters per minute (sccm), atomizer flow = 50 sccm, ultrasonic atomizer current = 0.6 A, print speed = 10 mm/s, and the substrate temperature = 80°C.

2.3. Intense pulse light sintering of printed silver film

The sintering of the printed silver nanoparticle film was carried out using a Xenon[™] S-1000 pulsed light system. The IPL sintering system consists of a tabletop controller, a sintering chamber, and an air-cooled lamp housing (Figure 1B). The lamp operating voltage ranges from 2.25 to 3.80 kV. The generated pulsed light has a pulse duration of 520 µs and a pulse energy ranging from 290 to 830 Joules/pulse depending on the lamp operating voltage. The in-house-made sintering chamber consists of a chamber that houses the sintering lamp and a height-adjustable stage. The chamber serves to prevent stray light from entering the lab and the height-adjustable stage allows for the adjustment of pulse light intensity by controlling the distance of the sample from the light source. As the light intensity varies spatially, all the test coupons are placed at the center of the stage and sintered with five light pulses to ensure consistency.

2.4. Characterization methodology

Characterization of the printed film was performed to generate information that can be used for the optimization

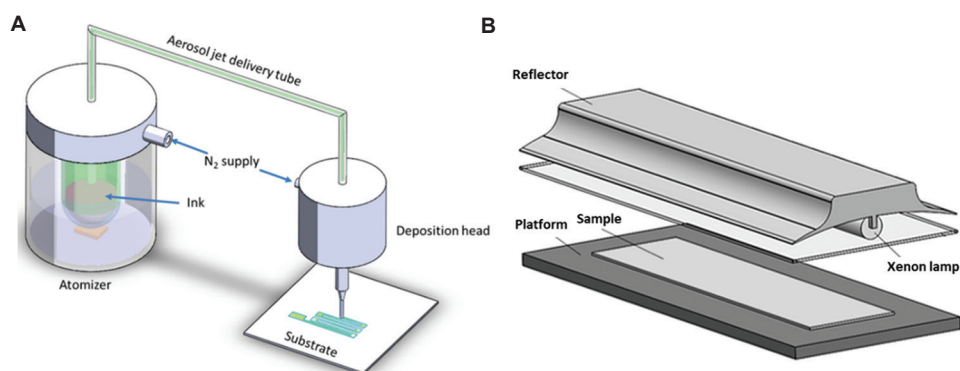


Figure 1. (A) Aerosol jet printing system (Reprinted with permission from^[40]. Copyright (2019) American Chemical Society. (B) Intense pulsed light system.

process. In this work, electrical property and the degree of delamination are the two main optimization objectives. As such, electrical property characterization and surface roughness characterization were conducted to provide information about the sheet resistance and the degree of delamination of the sintered film, respectively.

The electrical property was measured using a Lucas Labs Pro 4 collinear probe station with a Keithley 2400 source meter unit. The measurements were done with the collinear probes placed at the center of each printed circular film. In this work, sheet resistance was used to characterize the electrical property of the sintered film for a few reasons. First, it is almost impossible to calculate the resistivity of the sintered film with swelling and delamination morphology as the cross section of the film cannot be determined accurately using the equation $\rho = RA/L$ (R : resistance, A : cross-sectional area, and L : length) due to the non-uniform cross-sectional area^[32]. Second, as IPL sintering usually results in non-uniform sintering across the depth, sheet resistance was used in this study instead of electrical resistivity because sheet resistance is more meaningful in terms of reflecting the actual electrical property of the IPL-sintered films with different thicknesses. Furthermore, this allows electrical circuit designers and engineers to easily determine the number of print passes without the need for quantifying the film thickness.

The surface roughness characterization was performed using a Keyence VK-X200 confocal microscope coupled with a $\times 10$ magnification lens. The region of interest was selected to be at the center of the circular film. As the dimensions of a single scan region is approximately $1500 \mu\text{m} \times 1000 \mu\text{m}$, this can result in biased and selective sampling. To avoid this, a large scanning region was created by stitching nine different scan regions. This resulted in a scanned region with a dimension of $4500 \mu\text{m} \times 3000 \mu\text{m}$, which can better reflect the overall surface condition over the sintered film. The severity of the delamination can be

described by the surface roughness parameters. It should be noted that different surface roughness parameters are often used to describe different types of defects or surface anomaly. For instance, R_a measures the average deviation of the surface over a sampling area (Figure 2A), R_z measures the maximum deviation of the surface over a sampling area (Figure 2B), and R_{ku} measures the fourth power of the root mean square deviation to display the dimensionless fourth power of the sampling area (Figure 2C).

Each of these roughness parameters has its pros and cons in terms of describing the severity of the delamination. For example, R_a is useful for describing the overall severity of the delamination but difficult to pick up small or localized delamination, whereas R_z is useful for describing localized out-of-plane delamination but tend to overestimate the delamination severity of localized defects in relation to the overall surface condition. R_{ku} , on the other hand, is useful for differentiating different defect morphologies. As the delamination of the sintered film can happen in various ways, it is vital to use different surface roughness parameters such as R_a , R_z , and R_{ku} to account for the different modes of delamination. However, for the ease of the optimization process and analysis, a single surface roughness indicator is preferred over many different surface roughness parameters. As such, we have adopted a surface roughness indicator, S , as a linear sum of the normalized surface roughness parameters multiplied by their assigned weights. In this case, we defined the surface roughness indicator, $S = w_1 \tilde{R}_a + w_2 \tilde{R}_z + w_3 \tilde{R}_{ku}$ with $0 < S < 1$, $w_1 + w_2 + w_3 = 1$. Each surface roughness parameter was normalized with the highest values of respective surface roughness parameters ($R_{a,max} = 25.6 \mu\text{m}$, $R_{z,max} = 370.1 \mu\text{m}$, $R_{ku,max} = 172.0 \mu\text{m}$) within the sample populations, and the weights for each surface parameter are the same ($w_1 = w_2 = w_3 = 1/3$) to ensure equal contributions to the surface roughness indicator, S . To illustrate the correlation between the adopted surface roughness indicator and the

actual sintered film condition, six different sintered films obtained using different process parameters were used and their corresponding surface roughness was analyzed as shown in Figure 3. A qualitative comparison using reconstructed confocal scans of the sintered films can be found on Figure S1 of the supplementary document. The S value was calculated based on the equation as described

earlier. The surface roughness parameter for each coupon was obtained based on the average surface roughness parameters (R_a , R_z , and R_{ku}) of 3 regions of approximately equal size, as shown in Figure 3.

These six sintered films are randomly selected (from 105 samples) simply to illustrate the different types of delamination mode and severity. In general, the surface

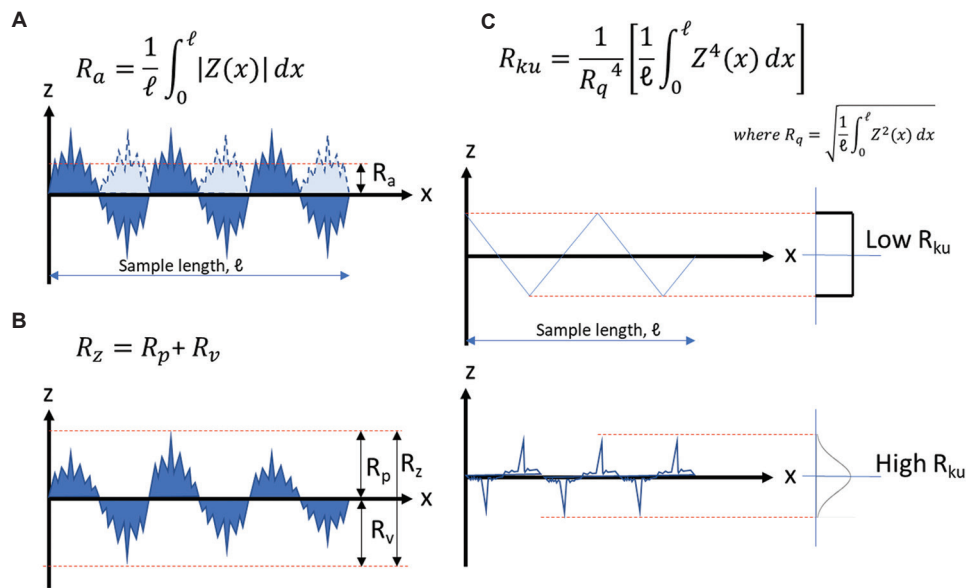


Figure 2. Definition of different surface roughness parameters. (A) R_a , (B) R_z , and (C) R_{ku} [41].

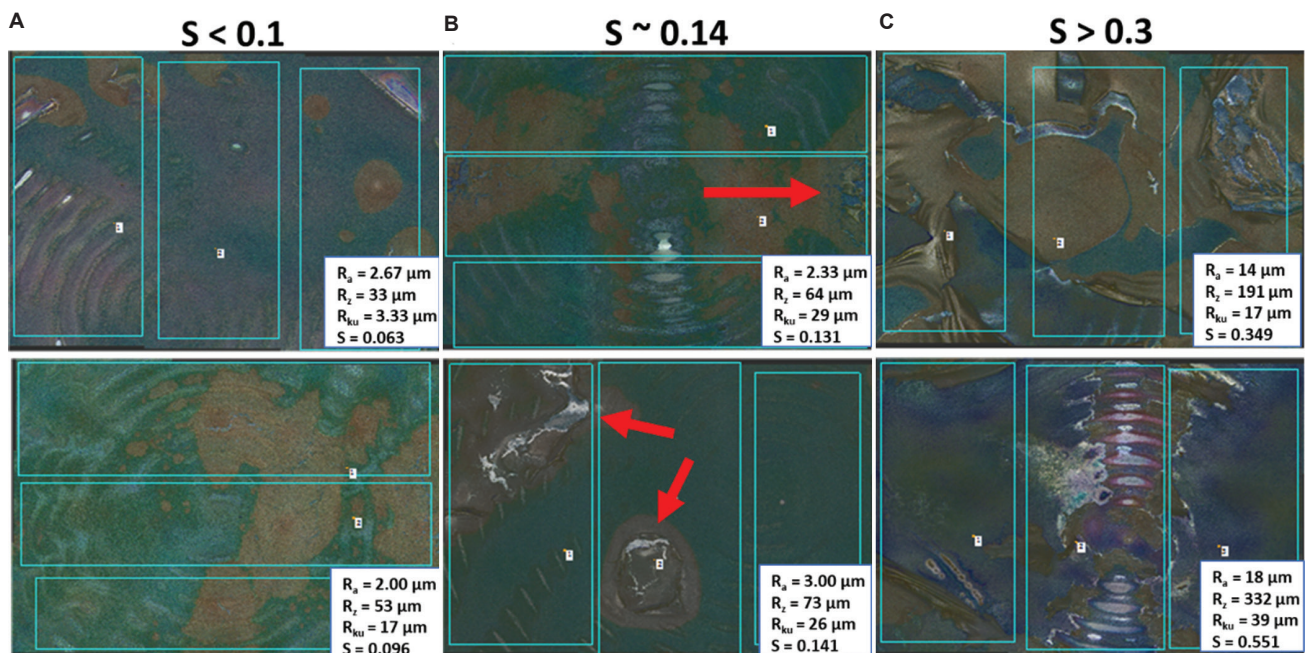


Figure 3. Correlation between surface roughness indicator and the severity of delamination of the sintered film. (A) Coupons with $S < 0.1$ contains no delamination, (B) coupons with $S \sim 0.14$ suffer mild delamination, and (C) coupons with $S > 0.3$ have severe delamination issue. Turquoise lines show the sub-sampling region for each coupon.

roughness indicator can be used to differentiate the delamination of sintered film effectively. For instance, for the sintered film with no obvious delamination, the surface roughness indicator normally falls below 0.1 ($S < 0.1$) as shown in the two optical images (two different coupons) in Figure 3A. For the moderately delaminated film which has small, localized delamination, they normally fall in the range between 0.1 and 0.25. Figure 3B shows the two different coupons that contain small, localized surface anomalies with a surface roughness indicator, S close to 0.14. Finally, Figure 3C shows the coupons with severe delamination issue with a surface roughness indicator value of higher than 0.3.

2.5. Design of experiment

To investigate the effect of the photonic sintering parameters on the conductive ink printed with different thicknesses, two factors were considered in this study, namely, (1) the sintering distance, which directly influences the light intensity received by the conductive ink, and (2) the number of layers of the conductive ink, which determines the thickness of the conductive film, t (Figure 4), were varied. The correlation between the number of printed layers and the film thickness can be determined using linear regression as shown in Figure 4. In essence, the greater number of print passes will lead to more material being deposited onto the substrate, resulting in thicker films. This correlation is useful for estimating the average electrical resistivity, ρ_{ave} of the sintered films with the obtained sheet resistance, R_s using the equation, $\rho_{ave} = R_s \cdot t$.

The conditions that were taken into consideration in this study are shown in Table 1. The conductive films were printed in different number of layers (1–5). Three samples

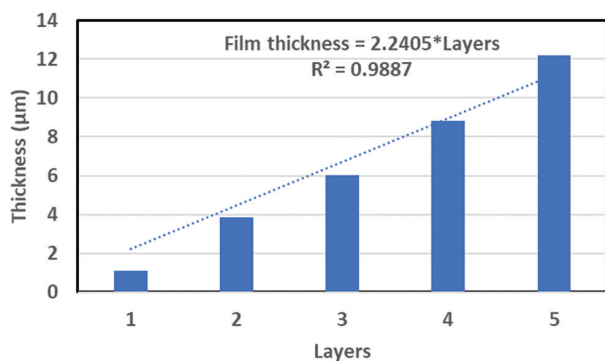


Figure 4. Relationship between film thickness and number of printed layers.

Table 1. Conditions considered in this study

Sintering distance (cm)	40, 45, 50, 55, 60, 65, 70
Number of layers	1, 2, 3, 4, 5

were printed for each film thickness (number of layers). For each film thickness, the sintering distance was varied from 40 to 70 with a step increment of 5 (7 levels). Hence, a total of 105 ($7 \times 5 \times 3$) samples were printed in this study.

2.6. A desirability function approach

Here, a desirability function approach was used to transform the two response variables (number of layers and sintering distance) into a single response variable function in 2D design space. The optimal sintering process parameters could then be effectively evaluated by minimizing the single response function. To assess the desirability of the contradicting responses quantitatively, each independent response y_i is converted into an individual desirability function, d_i . The desirability function, d_i , changes within the range [0,1], where $d_i = 0$ indicates the independent response y_i is beyond the satisfactory range, and $d_i = 1$ implies the independent response y_i achieves its target value. Depending on whether a specified response y_i is required to be reduced or increased, different desirability function d_i is utilized accordingly.

For minimizing a particular response, the desirability function can be quantitatively calculated by a Smaller-The-Better criteria (Eq. 1):

$$d_i = \begin{cases} 0 & y_i > U \\ \left(\frac{y_i - U}{L - U}\right)^r & L \leq y_i \leq U \\ 1 & y_i < L \end{cases} \quad (\text{Eq.1})$$

where U and L symbolize the maximum value and minimum value of a target response, respectively. r is the user-specified parameter ($r > 0$) to indicate the shape of desirability function d_i , discussion and descriptive figures on the different choices of r are described by Wang *et al.*^[42].

Then, the transformed individual desirability functions can be merged into a single response variable function (desirability function D) as shown in Eq. 2 to calculate the overall desirability of the contradicting responses:

$$D = \left((d_1)^{u_1} (d_2)^{u_2} \dots (d_n)^{u_n} \right)^{\frac{1}{\sum u_i}} \quad (\text{Eq.2})$$

where u_i are user-specified weights of the i -th response ($i=1, \dots, n$) and n is the number of individual responses. Following that, a statistical software Design-Expert® was used to ascertain the optimal process parameters by maximizing the single response of the overall desirability function.

2.7. GA-based multi-objective optimization

GA is a heuristic global optimization method inspired by the theory of biological evolution where the generated new

population can effectively receive the characteristics of the best solutions of the precedent^[43]. Besides that, due to capability of simultaneously evaluating a set of generations rather than individual solution, the GAs can converge fast and have been widely used in various research areas for multi-objective optimization^[44,45]. A GA usually consists of three key phases: crossover, mutation and selection. Specifically, during the multi-objective optimization process, the genetic operations of crossover and mutation can be utilized to encourage the variety of the generated offspring^[46]. Following that, the selection operator will be adopted to evaluate and choose best solutions from a set of generations. Although the methodologies of selection can be classified into different types, including tournament-based selection and proportional selection, a non-dominated sorting GA III (NSGA-III) was employed to optimize the conflicting responses in this research^[47,48], which reduced the contradiction between the responses in an objective manner.

The relationship between varying factors (number of layers and sintering distance) and the resulting responses (sheet resistance and surface roughness indicator) was formed by fitting the data using response surface method (RSM). The reduced cubic model and the reduced sixth model were used for the sheet resistance and the surface roughness indicator, respectively. For simplicity, surface roughness was used in place of surface roughness indicator for the rest of the discussion. The ANOVA technique was used to study the significance of the main effects (A: Sintering distance and B: Number of print layers) and the interactions on the responses. The probability of F value greater than calculated F value due to noise is indicated by P -value. $P < 0.05$ signifies the corresponding design parameter has effect on the mechanical property. ANOVA results (Table 2) reveal that both sintering distance and number of print layers have significant impact on the sheet resistance of the sintered film, registering P -value smaller than 0.0001 for the main effects. It was also noted that the interactions AB and AB² also registered $P = 0.0045$ and 0.0108, respectively, indicating there is a combined effect of the factors on the sheet resistance, or in other words, the effect of one factor is dependent on the level of the other factor.

For the surface roughness, ANOVA results (Table 3) reveal that both sintering distance and number of print layers have significant impact on the surface roughness of the sintered film, registering P -values of smaller than 0.0001 and 0.0009, respectively. It was found that most of the interactions were found to be significant up to the sixth order, with a few exceptions for A²B, A³B, B⁴, and A⁴B, registering $P = 0.3618$, 0.7594, 0.061, and 0.1762,

Table 2. ANOVA results for sheet resistance

Source	F-value	P-value
Model	44.50	<0.0001
A-Sintering distance	50.30	<0.0001
B-Print layers	128.39	<0.0001
AB	8.45	0.0045
A ²	0.5021	0.4803
B ²	3.48	0.0650
AB ²	6.75	0.0108
A _≥	4.39	0.0387
Residual		
Lack of Fit	1.07	0.3961
R ²	0.7625	
Adjusted R ²	0.7454	
Predicted R ²	0.7185	
Adeq Precision	21.7425	

respectively. The higher order of interactions indicates that the response is highly non-linear.

To check the model accuracy, the residuals of the derived models were computed by studentized residuals in standard deviation units. The normal probability of the studentized residuals for the target responses are presented in Figure 5, as the studentized residuals scattered along a straight line with little deviation, the modeling results are statistically acceptable. Furthermore, Figure 6 shows the model residuals versus test orders. As the residuals spread randomly around the center line without noticeable trend, they are considered independent from each other, thus excluding the effect of the test orders on the derived CCD models.

Figure 7 demonstrates the predicted sheet resistance and surface roughness versus actual printed sheet resistance and surface roughness, and the diagonal line drawn in Figure 7 is x (actual value) = y (predicted value). The high R² and Adeq. precision values suggests that the input-output relationship between the sintering process parameters and the sheet resistance and surface roughness are successfully recorded by the derived CCD models. Based on the ANOVA results, the input-output relationship for the responses of sheet resistance, R_s , and surface roughness, R_{SR} , with coded units for sintering process can be expressed as follows:

- $\ln(R_s \times 10^4) = -11.21 + 1.21A - 0.6126B - 0.2357AB + 0.0704A^2 + 0.1705B^2 - 0.3562AB^2 - 0.3894A^3$
- $\ln R_{SR} = -0.9469 + 2.45A + 0.7624B - 2.42AB + 2.53A^2 - 2.03B^2 - 0.5648A^2B - 1.36AB^2 - 5.94A^3 + 0.5038B^3 + 0.9995A^2B^2 - 0.5000A^3B + 3.04AB^3 - 11.02A^4 +$

Table 3. ANOVA results for surface roughness

Source	F-value	P-value
Model	41.00	<0.0001
A-Sintering distance	57.09	<0.0001
B-Print layers	11.86	0.0009
AB	13.17	0.0005
A ²	3.48	0.0657
B ²	18.74	< 0.0001
A ² B	0.8409	0.3618
AB ²	18.14	< 0.0001
A≥	30.57	< 0.0001
B≥	4.53	0.0362
A ² B ²	23.99	< 0.0001
A≥B	0.0944	0.7594
AB≥	23.35	< 0.0001
A ⁴	7.85	0.0063
B ⁴	3.61	0.0610
A≥B ²	15.63	0.0002
A ² B≥	2.69	0.1049
A ⁴ B	1.86	0.1762
A ⁵	12.60	0.0006
A≥B≥	17.61	< 0.0001
A ⁵ B	5.58	0.0205
A ⁶	7.32	0.0083
Residual		
Lack of Fit	1.82	0.0569
R ²	0.9121	
Adjusted R ²	0.8898	
Predicted R ²	0.8600	
Adeq Precision	21.2984	

$$0.7784B^4 + 1.51A^3B^2 - 0.6597A^2B^3 + 0.6386A^4B + 2.86A^5 - 3.16A^3B^3 + 2.70A^5B + 7.24A^6$$

where the high levels of the factors are coded as +1 and the low levels are coded as -1.

It can be seen from Figure 8A that the slope of the gradient for the sheet resistance over the number of print layers increases as the sintering distance becomes larger. It is observed that at lower number of print layers, the effect of the sintering distance on the sheet resistance is extremely prominent, in which larger sintering distance gives rise to higher sheet resistance. The effect becomes less prominent as the number of print layers increases.

The surface roughness does not scale linearly with the print layers nor the sintering distance (Figure 8B). A global peak is observed at print layer equal to three and sintering distance of 60 cm. The surface roughness drops sharply as the print layer reduces to 1 or sintering distance approaches 70 cm. The decrease is less drastic at higher print layers and sintering distance lower than 60 cm.

For high quality sintered film, both the sheet resistance and the surface roughness should be low. From Figure 9A, the sheet resistance is lowest in the region of high numbers of print layers and small sintering distance. The surface roughness, on the other hand, is lower at small number of print layers or at sintering distance of 70 cm (Figure 9B). The conflicting relationship results in a need to reach a compromise between the two parameters.

To identify the optimum condition for high quality sintered film, a desirability function approach was used (Eq. 2), where the multiple response variables were merged into a single response function established on a certain metric. In the overall desirability function, the weights of sheet resistance and surface roughness were initialized with the same value.

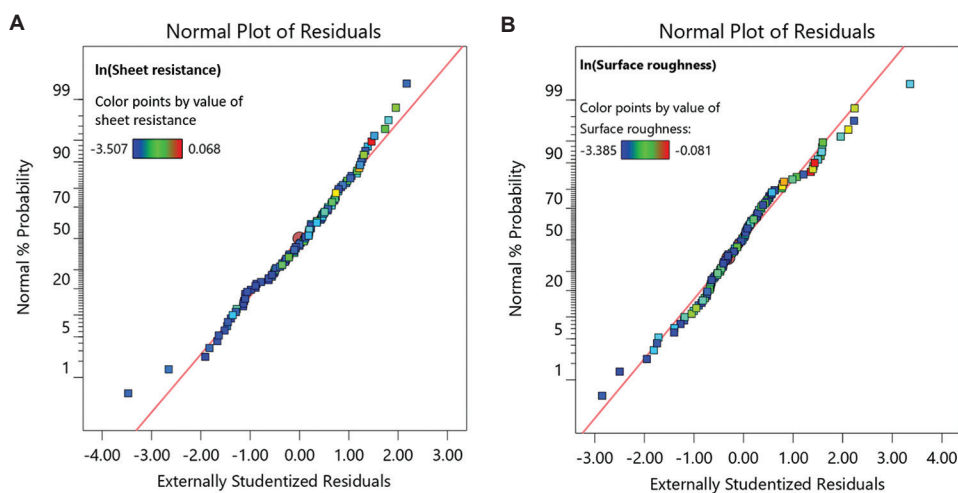


Figure 5. Normal probability plots of the residuals for (A) sheet resistance and (B) surface roughness.

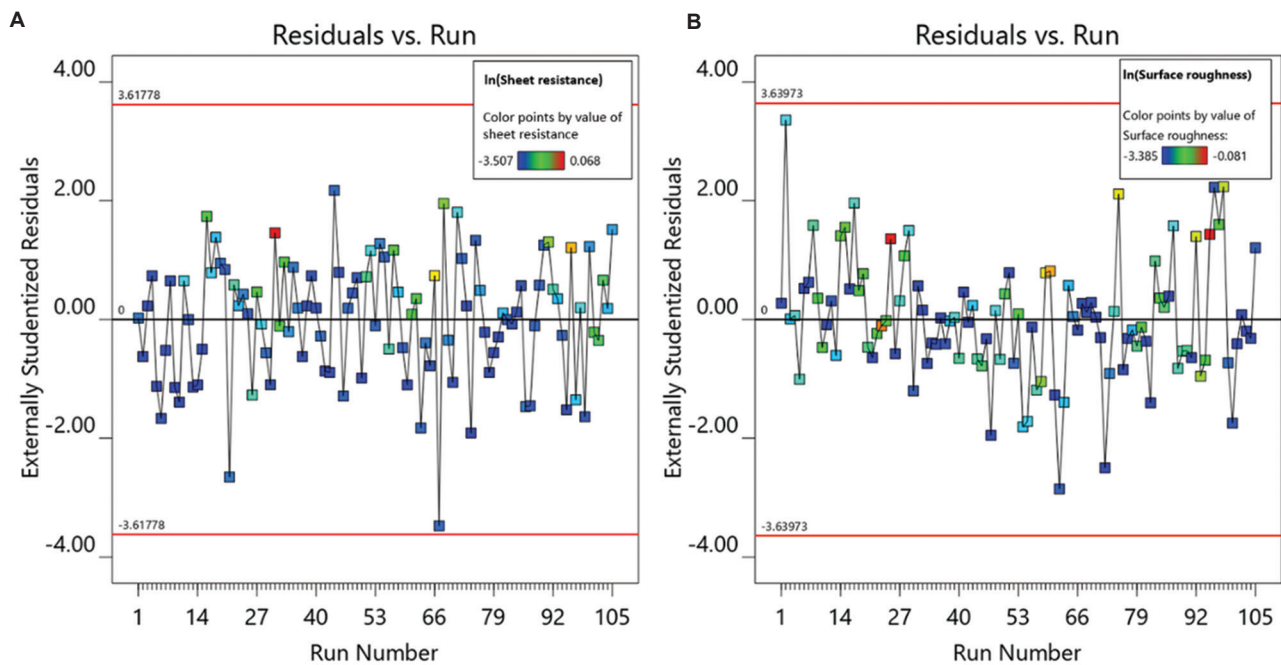


Figure 6. Model residuals versus test orders for (A) sheet resistance and (B) surface roughness.

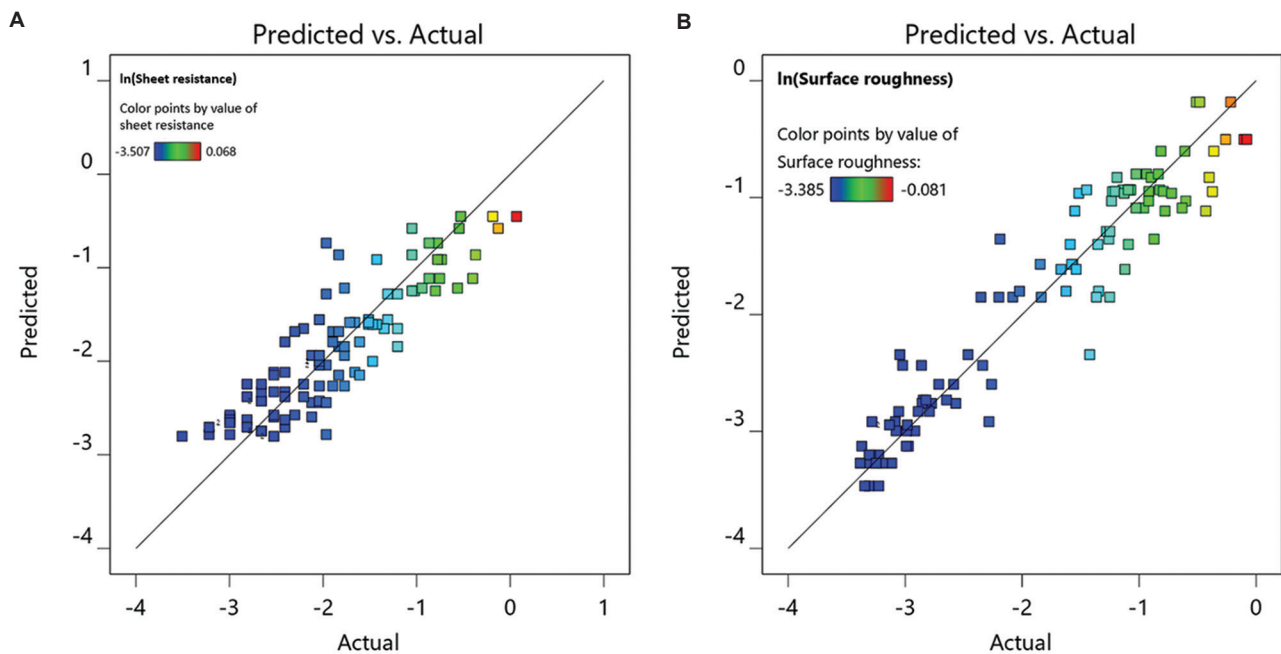


Figure 7. Predicted line values actual values for (A) sheet resistance and (B) surface roughness.

In addition, the minimum value and maximum value set for the sheet resistance and the surface roughness indicator are $[3 \times 10^{-2}, 1.07] \Omega/\text{sq}$ and $[0.034, 0.922]$, respectively. In this case, the optimal number of layer and sintering distance determined from the desirability function are 2 and 42.5 cm, respectively, and the overall desirability is 0.878 (Figure 10).

The desirability function approach can optimize the conflicting responses by merging the multi-objective vector into a single objective. As the attained optimal solution is very sensitive to the user specified weights used in the optimization process, there is a need to determine a set of Pareto-optimal points as alternate solutions in place of

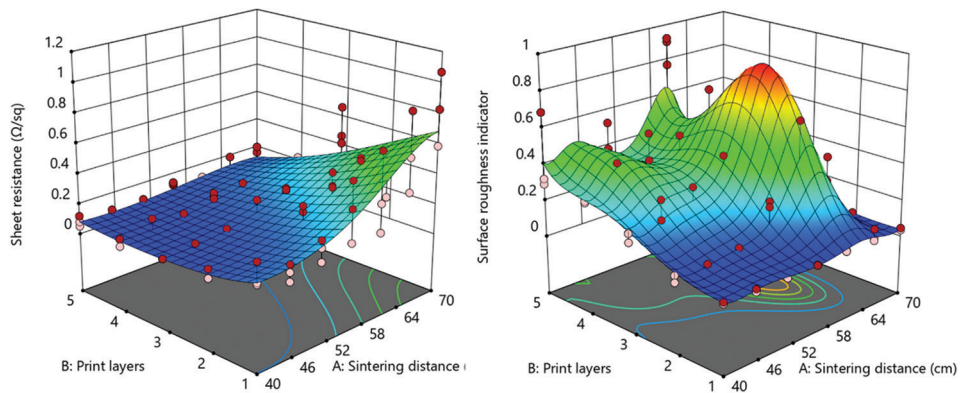


Figure 8. Response surface curves for (A) sheet resistance and (B) surface roughness with respect to the sintering distance and number of print layers.

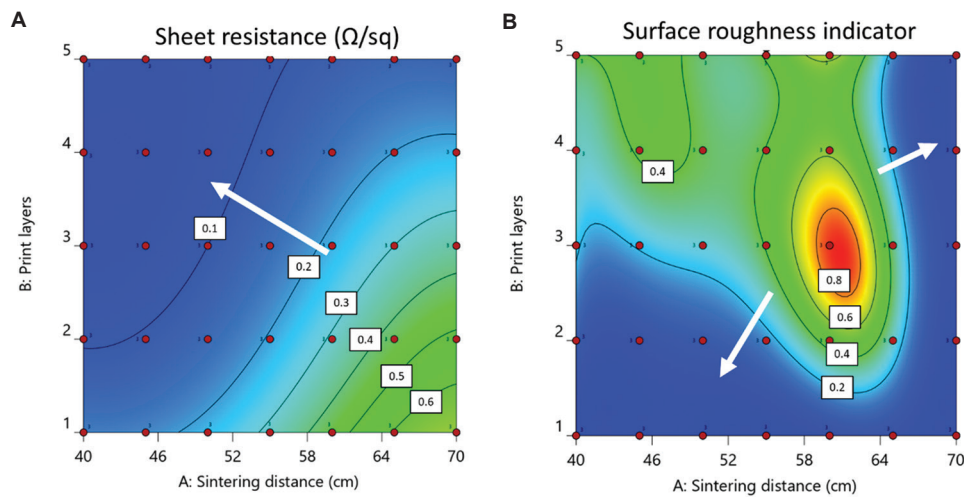


Figure 9. (A and B) Conflicting relationship between sheet resistance and surface roughness with respect to the number of print layers and the sintering distance in the sintering process. Arrow indicating the direction towards lower values.

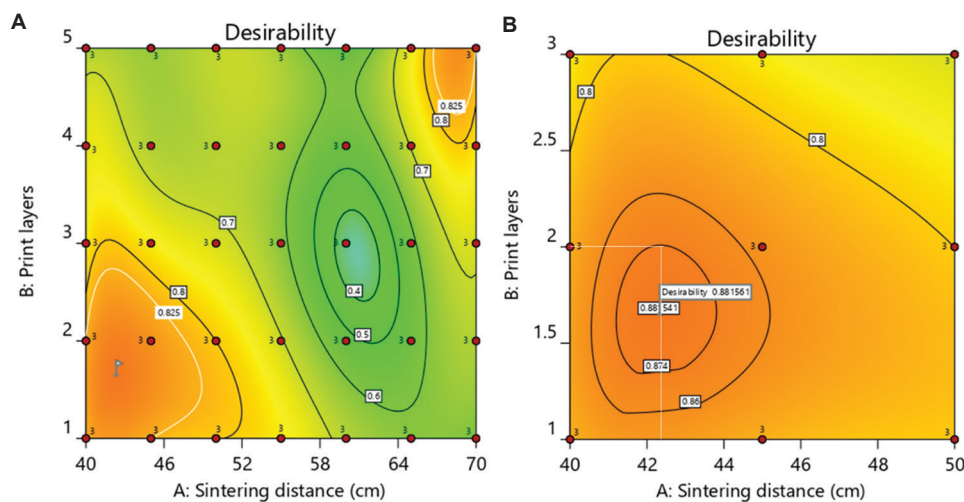


Figure 10. 2D map for the desirability function (A) over the entire studied process window and (B) zoomed in at the region with highest desirability. Red indicates high desirability and green indicates low desirability.

an individual point, particularly when prior knowledge about the underlying optimization problem is unknown. In this case, the derived statistical models were jointly driven with the NSGA-III to systematically optimize the conflicting responses in a more robust manner. Figure 11 demonstrates the flow chart of the adopted GA-based multi-objective optimization approach. During the optimization process, the input factors including sintering distance and number of print layers were characterized by the string of chromosome, and the proposed binary encoding of the chromosome pattern is shown in Figure 12, in which each process parameter looks like a gene that undergoes crossover and mutation in NSGA-III. Based on the experimental design and ANOVA results as discussed above, the attained statistical models were driven with the NSGA-III, and the two contradicting objectives (sheet resistance and surface roughness) were optimized in terms of minimization.

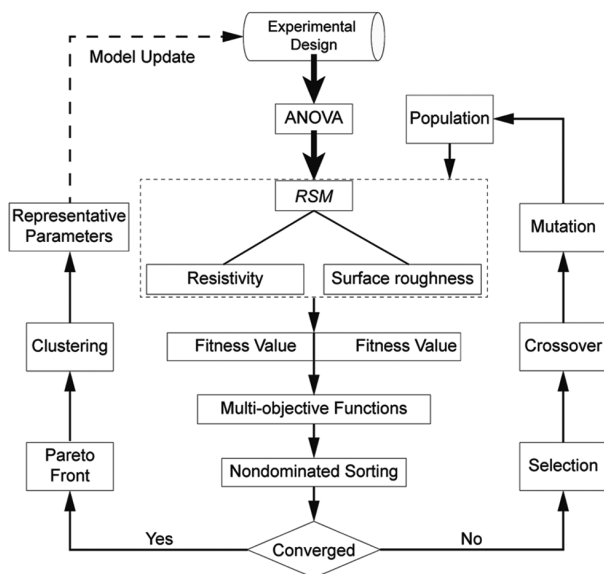


Figure 11. Flow chart of the adopted genetic algorithm-based multi-objective optimization approach.

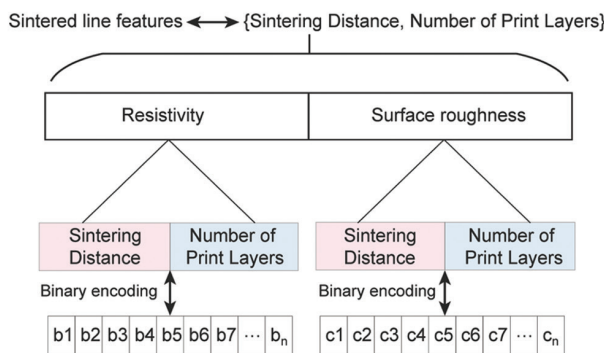


Figure 12. The chromosome encoding pattern in NSGA-III.

Table 4 summarizes the system settings of the adopted multi-objective optimization approach. Based on the proposed flow chart, the optimization process will be repeated if the employed NSGA-III does not reach its convergence. On the contrary, the convergent optimization algorithm will generate the corresponding Pareto front set as candidate solutions for the optimization process. However, as it will be inefficient to utilize the whole Pareto solution set during the evolution process, an affinity propagation approach is adopted to select the clustering centroids as representative solutions^[49], which will be helpful to further enhance the efficiency of the optimization process.

Figure 13 demonstrates the optimization results with respect to the conflicting relationship between the surface roughness and sheet resistance. As shown in Figure 13A-C, to ensure the convergence of the optimization process, the generations were increased until the obtained Pareto front remains stable. Under such circumstances, the corresponding Pareto optimal set based on clustering is shown in Figure 13D. Generally, the clustering centroids of the attained Pareto optimal set as shown in Table 5 can be selected as the representative solutions of the optimization process^[42], which will be helpful to extend the selection

Table 4. System settings of the adopted multi-objective optimization approach

Parameters	Settings
Number of input parameters	2
Number of statistical models	2
Objective functions	2
(1) Obj_1=sintering distance	Minimization
(2) Obj_2=number of print layers	Minimization
Constraints of adjustable parameters	2
(1) Sintering distance (cm)	[40, 70]
(2) Number of print layers	[1, 5]
Population size of NSGA-III	300
Crossover probability	0.9
Mutation probability	0.01
Maximal generations	2000

Table 5. Identified clustering centroids of the obtained Pareto optimal set

Solutions	Sintering distance (cm)	Number of print layers (→closest integer)	Sheet resistance (Ω/sq)	Surface roughness indicator
Solution 1	41.47	3.08 (→3)	6.31×10 ⁻²	0.168891
Solution 2	42.27	1.91 (→2)	7.42×10 ⁻²	0.09184
Solution 3	42.33	1.74 (→2)	9.30×10 ⁻²	0.04964

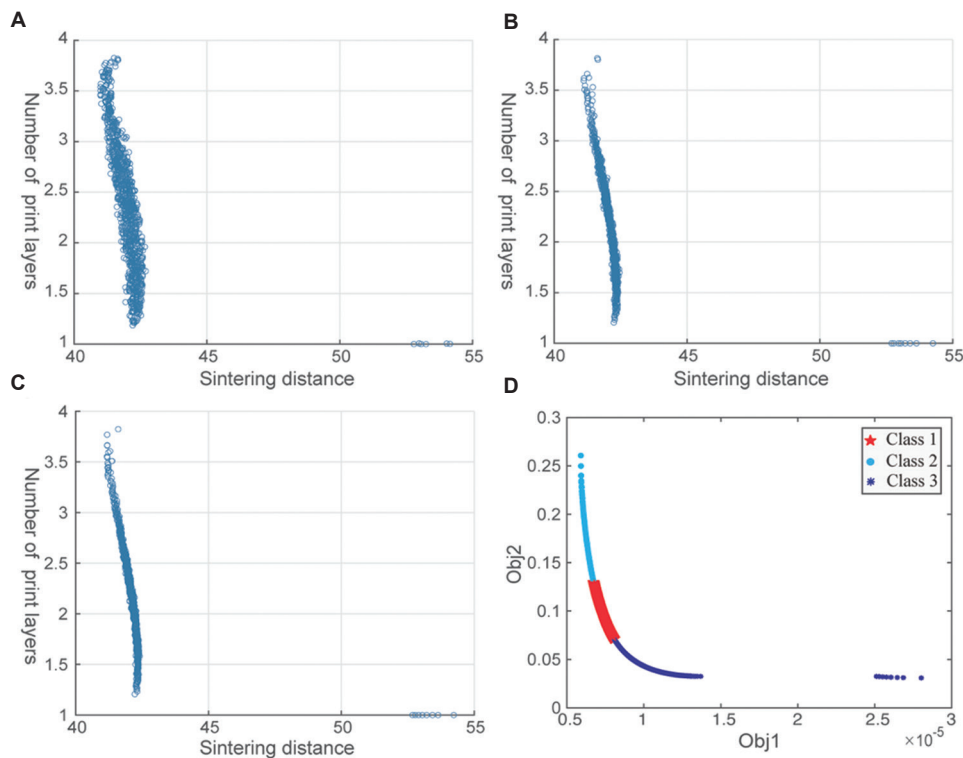


Figure 13. Optimization results with respect to sintered line features. (A-C) The variation of the obtained Pareto front under the generations of 500, 1000, and 2000, respectively. (D) The obtained Pareto optimal set corresponding to (C).

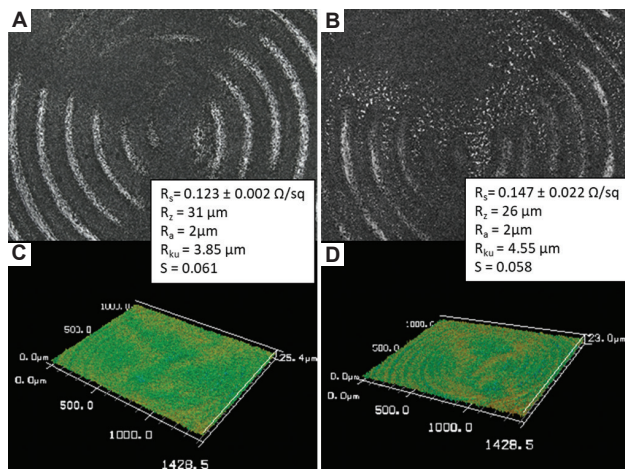


Figure 14. Optical images and confocal micrographs showing the surface morphologies of (A and C) Set 1 and (B and D) Set 2 as well as their corresponding surface roughness and sheet resistance.

for designers and optimize the printing quality in a more robust manner. However, as the number of print layers is limited to be an integer in this research, some approximate solutions such as (42.22, 2) and (41.50, 3) can be selected from the optimal Pareto front to replace the initial solutions, and more solutions from the selected cluster

could be used to further extend the selection. Compared with the desirability function, the non-dominated sorting-based multi-objective optimization approach can provide different selections according to users' preference, which will be beneficial to trade-off the conflicting responses in a more objective manner.

To verify the solutions, we have identified two solution sets that are close to the obtained Pareto optimal sets, which are Set 1 (sintering distance: 41.5 cm; print layers: 3) and Set 2 (sintering distance: 42.5 cm; print layers: 2). Figure 14 shows the optical images and the sheet resistance of the sintered silver film. The results suggest that the proposed approach can effectively identify a set of Pareto-optimal points for designers. Furthermore, the circuit designer could select the preferred solution from a set of Pareto-optimal solutions rather than from a single point, and the selection could be further extended from the cluster that the chosen solution represents, the surface morphology, and electrical property of the sintered film could be optimized in more robust and systematic manners.

3. Conclusion

In this work, a conflicting relationship between the electrical property and physical property of the photonic sintered silver thin film prepared using aerosol jet printing

technique is observed. As such, a hybrid multi-objective optimization approach is proposed to find the optimum solutions within the operating windows. In the proposed methodology, the response surface methodology is used to study the individual effects and their interactions of the main variables on the sheet resistance and the surface roughness of the printed silver film. The conflicting relationship between the sheet resistance and the surface roughness was ascertained by the RSMs. Then the 2D optimal operating windows were ascertained by a desirability function approach to reduce the inherent conflict of the print passes of the printed film and the sintering distance of the IPL sintering process. Thereafter, the derived RSMs and the corresponding statistical uncertainty were jointly driven with the NSGA-III to methodically optimize the overall printing quality in 2D space. The experimental results demonstrate that the suggested hybrid multi-objective optimization approach was advantageous to reduce the contradiction between the sheet resistance and the surface roughness, yielding printed films with low surface roughness and low sheet resistance.

Comparing to the conventional trial-and-error method, the suggested optimization methodology is found to be more efficient and systematic. It should be pointed out, however, that the optimal windows will vary significantly depending on the types of ink and substrate properties. Nevertheless, this work outlined a systematic approach for determining the optimal windows for the IPL sintering process of the aerosol jet printed films that can also be applied when other types of ink or substrate are used. For potential research work, the influence of the number of pulse and pulse duration can be systematically studied for aerosol jet printed silver film. Furthermore, this work outlines effective approaches for optimizing the electrical property and the surface morphology of the nanoparticle-based film which can potentially allow for the homogeneous deposition of material for the subsequent layers of multi-layered and multi-material electronics such as an electrochemical electrode with a dielectric passivation layer.

Acknowledgments

None.

Funding

This research is supported by the National Research Foundation, Prime Minister's Office, Singapore under its Medium-Sized Centre funding scheme and PUB, Singapore's National Water Agency under its Urban Solutions & Sustainability (Competitive Research Programme [Water] Scheme, PUB-1804-0075), and the Key Natural Science Project of Anhui Provincial Education Department (No. KJ2021A1111).

Conflict of interest

The authors declare no conflict of interest.

Author contributions

Conceptualization: Guo Liang Goh

Data curation: Guo Dong Goh

Funding acquisition: Wai Yee Yeong

Investigation: Guo Dong Goh

Methodology: Guo Liang Goh, Haining Zhang

Software: Haining Zhang

Supervision: Wai Yee Yeong, Tzyy Haur Chong

Writing – original draft: Guo Liang Goh, Guo Dong Goh

Writing – review & editing: Tzyy Haur Chong

References

1. Tan H, Tran T, Chua C, 2016, A review of printed passive electronic components through fully additive manufacturing methods. *Virtual Phys Prototyp*, 11: 271–288.
<https://doi.org/10.1080/17452759.2016.1217586>
2. Saengchairat N, Tran T, Chua CK, 2017, A review: Additive manufacturing for active electronic components. *Virtual Phys Prototyp*, 12: 31–46.
<https://doi.org/10.1080/17452759.2016.1253181>
3. Fisher G, Seacrist MR, Standley RW, 2012, Silicon crystal growth and wafer technologies. *Proc IEEE*, 100: 1454–1474.
<https://doi.org/10.1109/jproc.2012.2189786>
4. Tan HW, An J, Chua CK, *et al.*, 2019, Metallic nanoparticle inks for 3D printing of electronics. *Adv Electron Mater*, 5: 1800831.
<https://doi.org/10.1002/aelm.201800831>
5. Saidina D, Eawwiboonthanakit N, Mariatti M, *et al.*, 2019, Recent development of graphene-based ink and other conductive material-based inks for flexible electronics. *J Electron Mater*, 48: 3428–3450.
<https://doi.org/10.1007/s11664-019-07183-w>
6. Yang W, List-Kratochvil EJ, Wang C, 2019, Metal particle-free inks for printed flexible electronics. *J Mater Chem C*, 7: 15098–15117.
<https://doi.org/10.1039/c9tc05463d>
7. Bhat KS, Ahmad R, Wang Y, *et al.*, 2016, Low-temperature sintering of highly conductive silver ink for flexible electronics. *J Mater Chem C*, 4: 8522–8527.
<https://doi.org/10.1039/c6tc02751b>
8. Xu Z, Dong Q, Qtieno B, *et al.*, 2016, Real-time *in situ* sensing of multiple water quality related parameters using micro-electrode array (MEA) fabricated by inkjet-printing technology (IPT). *Sens Actuators B Chem*, 237: 1108–1119.
<https://doi.org/10.1016/j.snb.2016.09.040>

9. Zhang H, Moon SK, Ngo TH, 2020, 3D printed electronics of non-contact ink writing techniques: status and promise. *Int J Precis Eng Manuf Green Technol*, 7: 511–524.
<https://doi.org/10.1007/s40684-019-00139-9>
10. Goh GL, Zhang H, Chong TH, *et al.*, 2021, 3D printing of multilayered and multimaterial electronics: A review. *Adv Electron Mater*, 7: 2100445.
<https://doi.org/10.1002/aelm.202100445>
11. Goh GL, Ma J, Chua KL, *et al.*, 2016, Inkjet-printed patch antenna emitter for wireless communication application. *Virtual Phys Prototyp*, 11: 289–294.
<https://doi.org/10.1080/17452759.2016.1229802>
12. Goh GL, Shweta A, Yeong WY, 2018, High resolution aerosol jet printing of conductive ink for stretchable electronics. In: Proceedings of the 3rd International Conference on Progress in Additive Manufacturing (PRO-AM). Nanyang Technological University, Singapore, p109–114.
13. Agarwala S, Goh GL, Yeong WY, 2018, Aerosol jet printed pH sensor based on carbon nanotubes for flexible electronics. In: Proceedings of the 3rd International Conference on Progress in Additive Manufacturing (Pro-AM 2018), Singapore.
14. Goh GL, Agarwala S, Yeong WY, 2018, High resolution aerosol jet printing of conductive ink for stretchable electronics. In: Proceedings of the 3rd International Conference on Progress in Additive Manufacturing (Pro-AM 2018), Singapore.
15. Goh GL, Dikshit V, Koneru R, *et al.*, 2022, Fabrication of design-optimized multifunctional safety cage with conformal circuits for drone using hybrid 3D printing technology. *Int J Adv Manuf Technol*, 120: 2573–2586.
<https://doi.org/10.1007/s00170-022-08831-y>
16. Jiang P, Ji Z, Zhang X, *et al.*, 2018, Recent advances in direct ink writing of electronic components and functional devices. *Prog Addit Manuf*, 3: 65–86.
<https://doi.org/10.1007/s40964-017-0035-x>
17. Wilkinson N, Smith M, Kay R, *et al.*, 2019, A review of aerosol jet printing a non-traditional hybrid process for micro-manufacturing. *Int J Adv Manuf Technol*, 105: 4599–4619.
<https://doi.org/10.1007/s00170-019-03438-2>
18. Zeng M, Kuang W, Khan I, *et al.*, 2020, Colloidal nanosurfactants for 3D conformal printing of 2D van der waals materials. *Adv Mater*, 32: 2003081.
<https://doi.org/10.1002/adma.202003081>
19. Aleeva Y, Pignataro B, 2014, Recent advances in upscalable wet methods and ink formulations for printed electronics. *J Mater Chem C*, 2: 6436–6453.
<https://doi.org/10.1039/c4tc00618f>
20. Hoeng F, Denneulin A, Bras J, 2016, Use of nanocellulose in printed electronics: A review. *Nanoscale*, 8: 13131–13154.
<https://doi.org/10.1039/c6nr03054h>
21. Goh GL, Tay MF, Lee JM, *et al.*, 2021, Potential of printed electrodes for electrochemical impedance spectroscopy (EIS): Toward membrane fouling detection. *Adv Electron Mater*, 7: 2100043.
<https://doi.org/10.1002/aelm.202100043>
22. Jiang J, Bao B, Li M, *et al.*, 2016, Fabrication of transparent multilayer circuits by inkjet printing. *Adv Mater*, 28: 1420–1426.
<https://doi.org/10.1002/adma.201503682>
23. Agarwala S, Goh GL, Le TS, *et al.*, 2018, Wearable bandage-based strain sensor for home healthcare: Combining 3D aerosol jet printing and laser sintering. *ACS Sensors*, 4: 218–226.
<https://doi.org/10.1021/acssensors.8b01293>
24. Pan H, Ko SH, Grigoropoulos CP, 2008, Thermal sintering of solution-deposited nanoparticle silver ink films characterized by spectroscopic ellipsometry. *Appl Phys Lett*, 93: 234104.
<https://doi.org/10.1063/1.3043583>
25. Allen ML, Aronniemi M, Mattila T, *et al.*, 2008, Electrical sintering of nanoparticle structures. *Nanotechnology*, 19: 175201.
<https://doi.org/10.1088/0957-4484/19/17/175201>
26. Tan HW, Saengchairat N, Goh GL, *et al.*, 2020, Induction sintering of silver nanoparticle inks on polyimide substrates. *Adv Mater Technol*, 5: 1900897.
<https://doi.org/10.1002/admt.201900897>
27. Nam HJ, Kang SY, Park JY, *et al.*, 2019, Intense pulse light sintering of an Ag microparticle-based, highly stretchable, and conductive electrode. *Microelectron Eng*, 215: 111012.
<https://doi.org/10.1016/j.mee.2019.111012>
28. Jang YR, Joo SJ, Chu JH, *et al.*, 2020, A review on intense pulsed light sintering technologies for conductive electrodes in printed electronics. *Int J Precis Eng Manuf Green Technol*, 8: 327–363.
<https://doi.org/10.1007/s40684-020-00193-8>
29. Moores A, Goettmann F, 2006, The plasmon band in noble metal nanoparticles: an introduction to theory and applications, *New J Chem*, 30: 1121–1132.
<https://doi.org/10.1039/b604038c>
30. Kelly KL, Coronado E, Zhao LL, *et al.*, 2003, The optical properties of metal nanoparticles: The influence of size, shape, and dielectric environment. *J Phys Chem B*, 107: 668–677.
<https://doi.org/10.1021/jp026731y>
31. Zhang JZ, Noguez C, 2008, Plasmonic optical properties and applications of metal nanostructures. *Plasmonics*, 3: 127–150.
<https://doi.org/10.1007/s11468-008-9066-y>

32. Lee DJ, Park SH, Jang S, *et al.*, 2011, Pulsed light sintering characteristics of inkjet-printed nanosilver films on a polymer substrate. *J Micromech Microeng*, 21: 125023.
<https://doi.org/10.1088/0960-1317/21/12/125023>
33. Moon CJ, Kim I, Joo SJ, *et al.*, 2017, Flash light sintering of ag mesh films for printed transparent conducting electrode. *Thin Solid Films*, 629: 60–68.
<https://doi.org/10.1016/j.tsf.2017.03.049>
34. Kang J, Ryu J, Kim H, *et al.*, 2011, Sintering of inkjet-printed silver nanoparticles at room temperature using intense pulsed light. *J Electron Mater*, 40: 2268–2277.
<https://doi.org/10.1007/s11664-011-1711-0>
35. Niittynen J, Abbel R, Mäntysalo M, *et al.*, 2014, Alternative sintering methods compared to conventional thermal sintering for inkjet printed silver nanoparticle ink. *Thin Solid Films*, 556: 452–459.
<https://doi.org/10.1016/j.tsf.2014.02.001>
36. Hösel M, Krebs FC, 2012, Large-scale roll-to-roll photonic sintering of flexo printed silver nanoparticle electrodes. *J Mater Chem*, 22: 15683–15688.
<https://doi.org/10.1039/c2jm32977h>
37. Chung WH, Hwang HJ, Lee SH, *et al.*, 2012, *In situ* monitoring of a flash light sintering process using silver nano-ink for producing flexible electronics. *Nanotechnology*, 24: 035202.
<https://doi.org/10.1088/0957-4484/24/3/035202>
38. Yung KC, Gu X, Lee C, *et al.*, 2010, Ink-jet printing and camera flash sintering of silver tracks on different substrates, *J Mater Process Technol*, 210: 2268–2272.
<https://doi.org/10.1016/j.jmatprotec.2010.08.014>
39. Tobjörk D, Aarnio H, Pulkkinen P, *et al.*, 2012, IR-sintering of ink-jet printed metal-nanoparticles on paper. *Thin Solid Films*, 520: 2949–2955.
<https://doi.org/10.1016/j.jmatprotec.2010.08.014>
40. Goh GL, Agarwala S, Yeong WY, 2019, Aerosol-jet-printed preferentially aligned carbon nanotube twin-lines for printed electronics, *ACS Appl Mater Interfaces*, 11: 43719–43730.
<https://doi.org/10.1021/acsami.9b15060>
41. Keyence. Surface Roughness Parameters. Keyence. Available from: <https://www.keyence.com/ss/products/microscope/roughness/line/parameters.jsp> [Last accessed on 2021 Dec 20].
42. Zhang H, Choi JP, Moon SK, *et al.*, 2020, A hybrid multi-objective optimization of aerosol jet printing process via response surface methodology., *Addit Manuf*, 33: 101096.
<https://doi.org/10.1016/j.addma.2020.101096>
43. Srinivas M, Patnaik LM, 1994, Genetic algorithms: A survey. *Computer*, 27: 17–26.
44. Chen JH, Ho SY, 2005, A novel approach to production planning of flexible manufacturing systems using an efficient multi-objective genetic algorithm. *Int J Mach Tools Manuf*, 45: 949–957.
<https://doi.org/10.1016/j.ijmactools.2004.10.010>
45. Saravanan R, Asokan P, Sachidanandam M, 2002, A multi-objective genetic algorithm (GA) approach for optimization of surface grinding operations. *Int J Mach Tools Manuf*, 42: 1327–1334.
[https://doi.org/10.1016/s0890-6955\(02\)00074-3](https://doi.org/10.1016/s0890-6955(02)00074-3)
46. Jain NK, Jain V, Deb K, 2007, Optimization of process parameters of mechanical type advanced machining processes using genetic algorithms. *Int J Mach Tools Manuf*, 47: 900–919.
<https://doi.org/10.1016/j.ijmactools.2006.08.001>
47. Deb K, Pratap A, Agarwal S, *et al.*, 2002, A fast and elitist multiobjective genetic algorithm: NSGA-II. *IEEE Trans Evol Comput*, 6: 182–197.
<https://doi.org/10.1109/4235.996017>
48. Srinivas N, Deb K, 1994, Multiobjective optimization using nondominated sorting in genetic algorithms. *Evol Comput*, 2: 221–248.
<https://doi.org/10.1162/evco.1994.2.3.221>
49. Frey BJ, Dueck D, 2007, Clustering by passing messages between data points. *Science*, 315: 972–976.
<https://doi.org/10.1126/science.1136800>